Optics and Laser Technology 124 (2020) 105952

Contents lists available at ScienceDirect

Optics and Laser Technology

journal homepage: www.elsevier.com/locate/optlastec

All-fiber monostatic pulsed laser Doppler vibrometer: A digital signal processing method to eliminate cochannel interference

Shuping Peng[a], Shisong Wu[b,c,*], Yuanyang Li[b], Hongkai Chen[b,c]

[a] Zhejiang University of Technology, Hangzhou 310014, China
[b] State Key Laboratory of Laser Interaction with Matter, Changchun Institute of Optics, Fine Mechanics and Physics, Chinese Academy of Sciences, Changchun 130033, China
[c] Center of Materials Science and Optoelectronics Engineering, University of Chinese Academy of Sciences, Beijing 100049, China

HIGHLIGHTS

- An all-fiber monostatic pulsed LDV is developed.
- Cochannel interference is eliminated by the proposed range gated signal processing.
- The functions of range finding and vibrometry are realized at untra-low laser power output.

ARTICLE INFO

Keywords:
Laser Doppler vibrometer
Acoustic monitoring
Cochannel interference
Digital range gated signal processing

ABSTRACT

A 1.55 μm all-fiber monostatic pulsed laser Doppler vibrometer is developed to overcome demodulation failures caused by cochannel interference. We discussed the waveform design guidelines and proposed a digital range gated signal processing method to avoid the "Narcissus" effects. The resulting phase-modulated intermediate frequency (IF) of 40 MHz, which carries the information of target vibration, is demodulated down to the baseband using a specific in-phase and quadrature (I&Q) demodulator. An experiment is carried out at a 23 m standoff with pulse repetition interval of 50 ns, single pulse energy of 0.25 nJ, and pulse repetition frequency of 1 MHz to verify the performance of the prototype. The experimental results show that the pulsed LDV system has the ability to demodulate the acoustic vibration at a stand-off about several dozens of meters using an ultra-low output laser power.

1. Introduction

Laser Doppler vibrometer (LDV) is able to sense a small-amplitude vibration of the remote surfaces. The non-contact measurement benefits from the Doppler effects when light is reflected from a moving surface. Many Long-range applications have been successfully applied under an increasing number of situations where the aim is to extract the characteristics of the inaccessible vibrating target. Such applications ranges from mechanical diagnosis [1,2], military target identification [3], structural health monitoring [4–6], acoustic monitoring [7,8] and acoustic characterization [9,10]. As a rule of thumb, the noise floor level of the heterodyne system must be dominated by the shot noise originating from the Local Oscillator (LO) for optimum sensitivity operation [11]. However, the cochannel interferences (as mentioned in Ref[12]) can degrade the carrier-to-noise-ratio (CNR) which determines the performance of the vibrometer. Because the internal reflections in the system (also mentioned as "Narcissus" effects[13]) overwhelm the shot noise so that the internal parasitic reflections play a more important role than the shot noise. Such interferences can be mitigated by misaligning the pivotal optical surface a little in a free-space monostatic architecture (a configuration where the transmitter and receiver are situated at the same location) [14]. Benefited from modern miniaturization and the digitalization of characterization instruments, the system of the LDV utilizes off-the-shelf fiber optical device in fiber sensing to suffice a more stringent SWaP (size weight and power) constraint [15]. In a fiber-based arrangement, the interferences can be eliminated by adopting a bistatic configuration, but it increases the cost of the whole system dramatically [13,16–18]. As for a monostatic pulsed architecture, Ref[19] utilized a diode switch to separate returns from the internal parasitic reflections which mainly comes from the

* Corresponding author at: State Key Laboratory of Laser Interaction with Matter, Changchun Institute of Optics, Fine Mechanics and Physics, Chinese Academy of Sciences, Changchun 130033, China. Center of Materials Science and Optoelectronics Engineering, University of Chinese Academy of Sciences, Beijing 100049, China
E-mail address: wushisong15@mails.ucas.ac.cn (S. Wu).

https://doi.org/10.1016/j.optlastec.2019.105952
Received 30 August 2019; Received in revised form 1 November 2019; Accepted 11 November 2019
Available online 12 December 2019
0030-3992/ © 2019 Elsevier Ltd. All rights reserved.

fiber end in a wind coherent Doppler radar. However, it's hardware-dependent and band-limited. Additionally, the target returns and internal reflections are temporally divided sparse and they are easy to separate from each other. When the sensing distance comes shorter, it becomes far more difficult to separate. That is why an all-fiber monostatic LDV is never applied in medium range sensing.

In this paper, we proposed a digital range gated signal signal processing method to separate the target returns from parasitic reflections in a pulsed monostatic vibrometer. Section 2 introduces the principle and system design of monostatic pulsed vibrometer including signal modeling, waveform design, range gated signal processing, I & Q demodulation and the analysis of CNR and SNR. Section 3 details vibrometer architecture and the two-functional ability: range finding and vibrometer. Finally, conclusions are given in Section 4.

2. Monostatic pulsed laser Doppler vibrometer

The principle and implementation of our self-developed all-fiber pulsed laser Doppler vibrometer is presented hereafter. Section 2.1 describes the principle of the pulsed LDV and models the return signal considering the system internal reflections. Since the failure of demodulation due to the light reflectivity from the fiber end or circulator, a range gated signal processing method has been proposed to deal with the corrupted IF signal. This method is described in Section 2.2. Section 2.3 details the I & Q demodulator in our LDV implementation. An easy-understanding graphic interpretation of the SNR and CNR is explained in Section 2.4.

2.1. Principle and signal modeling

As depicted in Fig. 1, the principle of the coherent heterodyne vibrometer depends on the Doppler shift or phase shift which is introduced by the vibration of the target when light is back-reflected from its surface. The light beam from a single-mode laser with a narrow line width is split into two paths. One with the little power is served as a LO, the other with the most power is frequency-shifted by an Acousto-optical Modulator (AOM). In order to operate in pulsed mode, the radio-frequency (RF) driver of the AOM is usually driven by a pulsed voltage series. The pulsed measurement beam is expanded and then focused onto the vibrating surface to a diffraction limited spot. Back-scattered light from the focused spot is then collected by the same optics and transformed into a mostly collimated beam. The parasitic reflection and scattered light both mixed the LO in the photodetector. The analytical

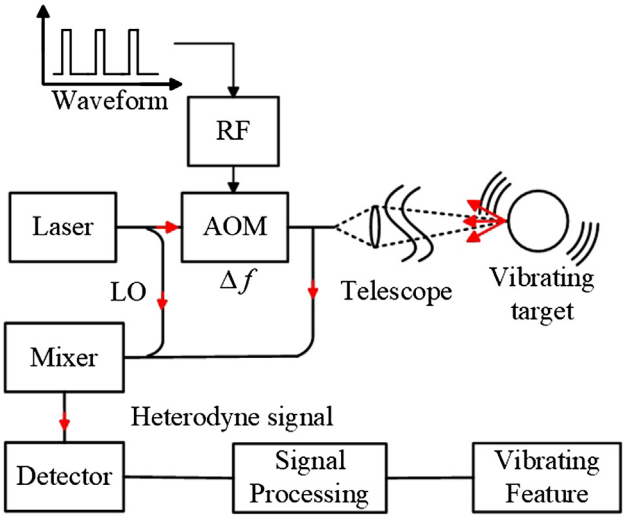

Fig. 1. Diagram of a pulsed heterodyne laser Doppler vibrometer, modulating the voltage of the AOM RF driver to implement the pulse mode.

expression of the pulsed LDV photocurrent is modeled in the following.

The AOM is usually utilized to operate in a heterodyne configuration. The heterodyne detection scheme enables the discrimination of movement direction and the suppression of high frequency noise. The return signal from the diffuse surface illuminated by a pulsed transmitted laser beam considering the parasitic reflection is given by

$$\begin{aligned} E_S(t) = {} & \mu(t)\gamma E_t Re\{\exp[j(\omega_0+\omega_{IF})t - j\Phi(t)]\} \\ & + m[\tau(t)]\mu[t-\tau(t)]E_t Re\{A_s(t)\exp[j\Phi_s(t)] \\ & \times \exp[j(\omega_0+\omega_{IF})[t-\tau(t)] + j\Phi[t-\tau(t)]]\} \end{aligned} \tag{1}$$

where $\mu(t)$ is the amplitude modulation applied to the RF driver of the AOM; γ is the percentage of reflected energy; $m[\tau(t)]$ is the power attenuation according the radar equation; E_t is light field vector of transmitted light; ω_0 and ω_{IF} are the frequency of light and the frequency shift introduced by AOM; $A_s(t)$ and $\Phi_s(t)$ are the speckle-induced amplitude and phase fluctuations respectively; $\Phi(t)$ is the laser phase noise, and $\tau(t)$ is the time delay due to the round-trip path variation. Here we adopted a continuous light as an LO of the form

$$E_{LO}(t) = E_{LO} Re\{\exp[j(\omega_0 t - \Phi(t))]\} \tag{2}$$

Then, photocurrent of the square law detector is of the form

$$i(t) = i_{\mathrm{LO}} + i_{\mathrm{S}}(t) + i_{IF}(t) + n(t) \tag{3}$$

where E_{LO} is light field vector of LO light; η_h is the heterodyne efficiency, $n(t)$ is the shot noise. The IF signal under a shot-noise limited situation is expressed as

$$\begin{aligned} i_{IF}(t) = {} & 2\eta_h E_{LO} E_t \mu(t)\gamma Re\{\exp[j\omega_{IF} t]\} \\ & + 2\eta_h E_{LO} E_t \mu[t-\tau(t)]m[\tau(t)] \\ & \times Re\{A_s(t)\exp[j\omega_{IF}[t-\tau(t)] + j\omega_0\tau(t)] \\ & \times \exp[\mathrm{j}(\Phi_{\mathrm{p}}(\mathrm{t}) - \Phi_{\mathrm{s}}(\mathrm{t}))]\} \end{aligned} \tag{4}$$

where $\Phi_p = \Phi(t) - \Phi(t-\tau(t))$ is the laser phase noise difference between the LO signal and delayed return signal. The first term in Eq. (4) refers to the representation of parasitic reflection in IF, while the second term in Eq. (4) represents the vibrating characteristics of the target. They are separated from each other temporally due to the time delay $\tau(t)$. In order to eliminate the impairment of the parasitic reflection, the useful information of the vibration is selected by a range gated signal processing method, then the intermediate frequency signal is down-converted to the baseband signal. This algorithm is detailed in the next subsection.

The time delay $\tau(t)$ can be expressed by

$$\tau(t) = \frac{2R(t)}{c} = \frac{2}{c}[R_0 + vt + X(t)] = \tau_0 + \frac{2}{c}[vt + X(t)] \tag{5}$$

where τ_0 is the initial time delay, v is the line-of-sight (LOS) velocity of the target, $X(t)$ is the simple piston motion of the target surface. Assuming the bulk Doppler shift due to LOS velocity is perfectly compensated, the ideally phase of the baseband signal becomes

$$\theta(t) = \frac{4\pi X(t)}{\lambda} - \Phi_s(t) + \Phi_p(t) \tag{6}$$

As for a simple piston motion the variation of the signal is of the form

$$\frac{4\pi X(t)}{\lambda} = \frac{4\pi A_{vib}\cos(\omega_m t)}{\lambda} = \beta\cos\omega_m t \tag{7}$$

with modulation index $\beta = 4\pi A_{vib}/\lambda$ and radian vibration frequency $\omega_m = 2\pi f_m$. Considering the discussions above, the IF output finally becomes

$$\begin{aligned} i_{IF}(t) = {} & 2\eta_h \gamma E_{LO} E_t(t) m(\tau_0)\mu(t-\tau_0)A_s(t) \\ & \times Re\{expj[\omega_{IF} t + \theta(t)]\} \\ & = 2\eta_h \gamma E_{LO} E_S(t) Re\{expj[\omega_{IF} t + \theta(t)]\} \\ & = A(t)\sum_{n=-\infty}^{+\infty} J_n(\beta)cos[(\omega_{IF} + n\omega_m)t + \Phi_p(t) - \Phi_s(t)] \end{aligned} \tag{8}$$

where $E_S(t)$ is the return light amplitude fluctuation, $A(t)$ is the total

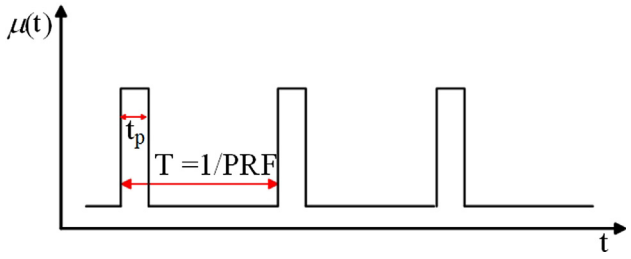

Fig. 2. Parameters of pulse waveforms in amplitude modulation $\mu(t)$: t_p, pulse width; T, pulse repetition interval; PRF, pulse repetition frequency.

current fluctuation, $J_n(\beta)$ is the Bessel function of the first kind, $n = 0, \pm1, \pm2\cdots$. For small amplitude with $\beta \ll 1$, the energy mainly focused at the sidebands $\omega_{IF} \pm \omega_m$.

2.2. Waveform design and range gated signal processing

Pulsed vibrometer benefits from the existing techniques in radar signal processing including waveform design. The pulse-pair waveforms and polypulse waveforms are successfully applied to super-long-range vibration sensing [18], but are no more appropriate for acoustic monitoring at a short or medium range. We now discuss the constrains that apply on waveform parameters in order to choose a suitable waveform for acoustic monitoring. (i) The pulse repetition frequency PRF has to satisfy the Nyquist criterion for correct sampling, PRF > $2f_{vib,max}$. Because the information of the speech ranges 300 Hz to 3 kHz, the minimum PRF is 6 kHz theoretically. In practice, the main energy of the excited vibrating surface is concentrated from 300 Hz to 500 Hz, so the claims of PRF can be loose. (ii) The pulse width, t_p (shown in Fig. 2 graphically),is determined by the frequency shift of the AOM f_{IF} and the time response of the AOM (rise-time t_{rise} and fall-time t_{fall}). The pulse width must be longer than the sum of the rise-time and the fall-time of the AOM ($t_p \geqslant t_{rise} + t_{fall}$), and also be several times of the reciprocal of the AOM frequency shift ($t_p \geqslant n/f_{IF}$, $n \geqslant 2$). (iii) The maximum and minimum operating distance is relevant to the PRF and the pulse width, $t_p \cdot c/2 \leqslant R \leqslant T \cdot c/2$, where T = 1/PRF is the pulse repetition interval, c is the speed of light. These constraints must be set considering the electrical characteristics of the specific AOM, the operation range as well as the noise condition.

The digital signal processing method presented below implements a range signal gating as a part of the IF signal pre-conditioning before the I & Q demodulation. As shown in Fig. 3(a), the IF signal is first matched-filtered to enhance the waveforms for better envelope detecting [20]. Then the matched filtered output is put into an asynchronous Hilbert complex envelope detector, which is graphed in Fig. 3(b). A finite impulse response (FIR) Hilbert transformer is used in the digital envelope detector to generate the analytic signal for the input of the Range Gated Signal Generator. The Delay element, whose time delay is equal to the Hilbert transformer's group delay, measured in samples, is required to achieve discrete signal synchronization [21]. After summing the absolute values of the real and imaginary part of the analytic signal respectively, the envelope is obtained by passing through an average low-pass filter. The main waveforms in the pre-processing diagram is pictured in Fig. 3(c). The envelope is first peak-searched during one pulse repetition interval. The envelope of the parasitic reflection in the system is amplitude-static compared with a varying amplitude envelope of the target returns. Then, the time delay between the two peaks, which is an estimation of the round-trip delay, can be calculated easily. A digital gate signal is generated at the position of the peak of the target envelope with a given pulse width. After group delay (due to delay element and the low-pass filter in Fig. 3(b)) compensation, the exact gate signal is multiplied with the matched-filtered output. Finally, the range gated signal is obtained.

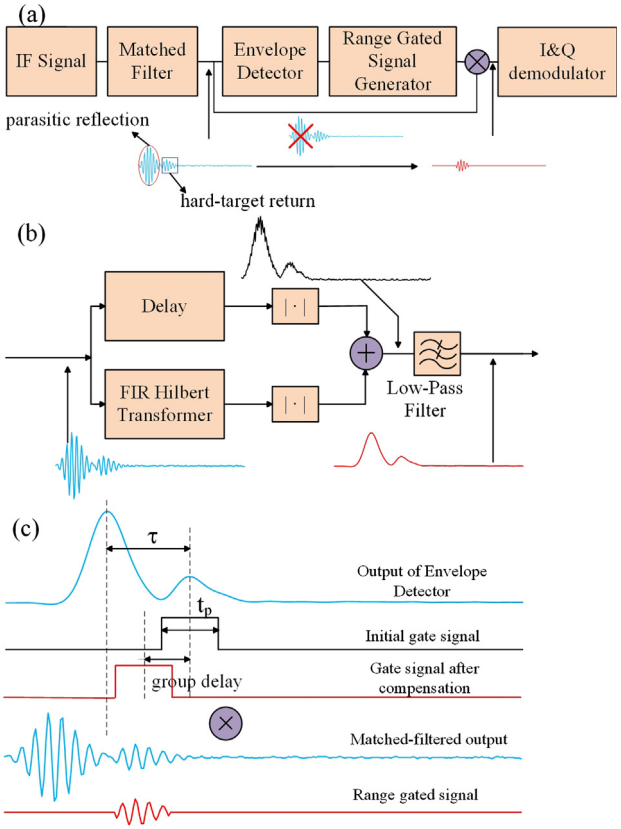

Fig. 3. (a) Diagram of IF signal pre-processing. The parasitic reflection is circled in red and the hard-target return is bracketed in black on the matched-filtered IF signal respectively (b) Details about Asynchronous Hilbert complex envelope detector in (a). (c) Waveforms in the diagram for generating the range gated signal.

2.3. I &Q demodulation

I & Q demodulation technique [22] is the best scheme for remote monitoring of vibrations, because it is independent of amplitude fluctuations caused by the target characteristics, atmospheric turbulence attenuation and speckle evolution [13]. The digital strategy needs no more calibrations for I and Q channel. The improved I & Q demodulator is graphed in Fig. 4. In a traditional I & Q demodulator, a downsampling decimator is always used after the cascaded integrator-comb (CIC) filter in digital down convertor (DDC). However, the input of the demodulator is pulsed and not a continuous one, so the decimator may peak up the non-pulse region and lose the information. Therefore, after passing through a low-pass filter, the signal is buffered into a matrix of size $N \times M$, N is the samples during one pulse repetition interval. Because the pulse region in the range gated signal is delayed by a group delay of the low-pass filter, it is important to compensate the group delay to the pulse region for determining the row number in the fast-time axis of the matrix. By selecting a whole row of the matrix, the N-times down-sampled I & Q channel signals in the slow-time direction which contain the Doppler information are further low-pass filtered to remove the wide-band noise and then demodulated by the arctangent function before phase unwrap.

2.4. CNR and SNR

The performance of the vibrometer is determined by its noise floor, which consists of shot noise and speckle noise[23]. Speckle noise, also named multiplicative noise, occurs when laser spot moves with respect to a rough surface transversely due to pointing jitter or atmospheric drift [24]. Dräbenstedt [25] measures the translation-induced speckle

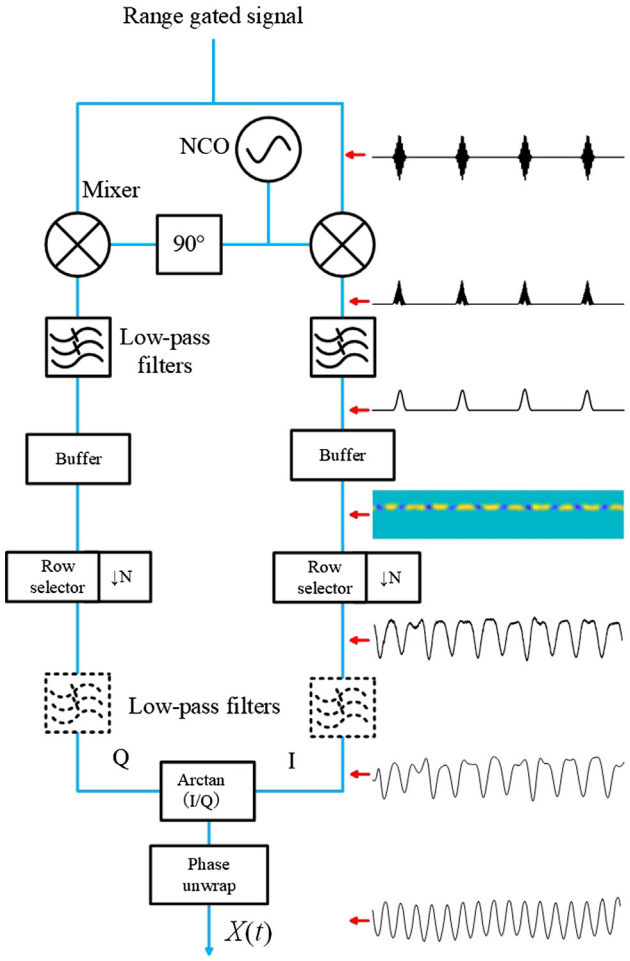

Fig. 4. I & Q demodulator for pulsed LDV. The range gated signal is first mixed with the numerically controlled oscillator (NCO) to generate pulsed I & Q signals. A low-order low-pass digital Fir filter filtered the I & Q signals to extract the pulse envelope. The envelopes are buffered and downsampled by the row selector. The antialiasing low-pass filter with a bandwidth B further filtered out the out-of-band noise.

noise floor at high CNR and found that exchange rate of the speckle pattern splits the spectrum into two regions and Leaf A. Jiang [23] extended them into three regions: constant below exchange rate, speckle dominated region and shot noise dominated region [26]. Hereafter, the impair of the speckle is not taken into consideration due to the small translation of the light spot on vibration surface.

The Fourier transform of Eq. (8), at frequency ω_{IF}, equals to $a + n$, where

$$a \equiv |A(t)|\exp[j\theta(t)] = 2\eta_h E_{LO} E_S(t)\exp[j\theta(t)] \tag{9}$$

is the carrier and n is the noise. Assume that the noise n is a two-dimensional Gaussian distribution with probability density function $\exp[-(r^2 + i^2)/(2n_{rms}^2)]/(2\pi n_{rms}^2)$, which is illustrated in Fig. 5(a). Therefore, the magnitude of noise is Rayleigh distributed. In the complex plane, the conventional representation of $\theta(t)$ is a phasor which is a victor sum of carrier a and random phaser sum n. The circle edge of the green color region with radius n_{rms} denotes the standard deviation. The variance of the rms value of $|n|$ is $n_{rms}^2 = 2qi_{LO}B$, where B is the single-sided bandwidth of the final low-pass filter in Fig. 4.

The CNR is usually obtained from the power spectrum of the IF current signal by $(peak - backgroud)/backgroud$, which can be expressed as

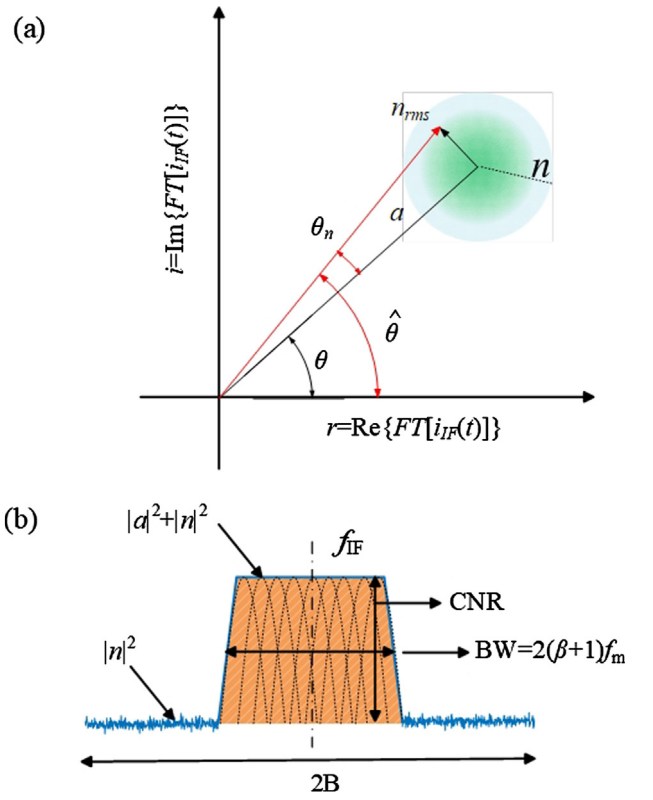

Fig. 5. (a) $i_{IF}(t)$ Fourier transform at ω_{IF} to illustrate a phasor diagram for carrier and noise. The noise n is two-dimensional Gaussian distributed with probability density function $\exp[-(r^2 + i^2)/(2n_{rms}^2)]/(2\pi n_{rms}^2)$.The rms of $|n|$ is determined by the antialiasing filter bandwidth in Fig. 4, $n_{rms}^2 = 2qi_{LO}B$. θ_n is the minimum detectable radian angle, θ is the true value of the peak-to-peak vibration radian angle and the $\hat{\theta}$ is the estimation of θ. (b) IF Spectrum diagram centered at f_{IF}. the peak deviation of the IF forms the vibration bandwidth $BW = 2(\beta + 1)f_m$ accumulatively. The height of the difference between the peak $|a|^2 + |n|^2$ and backgroud $|n|^2$ is the definition of the CNR.

$$\text{CNR} \equiv \frac{\text{carrier power}}{\text{noise power}} = \frac{E[|a|^2]}{n_{rms}^2} = \frac{2\eta_h^2 E_S^2}{qB} \tag{10}$$

where $E[\cdot]$ represents the expectation value during measurement, q is the electron charge. In other words, the CNR is obviously observed by the height of the difference between IF ($|a|^2 + |n|^2$) and noise ($|n|^2$). As shown in Fig. 5(b), the signal bandwidth, $BW = 2(\beta + 1)f_m$, is observed during a sweep time in the RF spectrum analyzer. According to the Carson's rule or a simple rule of thumb, the antialiasing filter bandwidth must be greater than the signal bandwidth ($B > BW$). The minimum detectable angle or the standard deviation of the carrier-plus-noise phaser $\hat{\theta}$ is

$$\theta_n \backsim \frac{n_{rms}}{E[|a|]} = \frac{1}{\sqrt{CNR}} \tag{11}$$

In the case of high CNR ($|a| \gg |n|$), assume the shot noise spectrum for $\hat{\theta}$ is flat over the bandwidth from $-B$ to $+B$, the variance of $\hat{\theta}$ is

$$(\theta_n)^2 = \int_{-B}^{+B} S_\theta(f)\mathrm{d}f = 2B{\cdot}S_\theta(f) \tag{12}$$

substitute Eq. (11) into Eq. (12) solving for $S_\theta(f)$ yields

$$S_\theta(f) = \frac{(\theta_n)^2}{2B} = \frac{1}{2B{\cdot}\text{CNR}} \tag{13}$$

for $-B \leqslant f \leqslant +B$ and zero otherwise. The surface displacement spectrum is therefore

$$S_x(f) = \left(\frac{\lambda}{4\pi}\right)^2 S_\theta(f) \qquad [m^2/Hz] \tag{14}$$

according the Eq. (6) in absence of speckle and laser phase noise ($\theta = 4\pi X/\lambda$). The single-sided displacement amplitude noise spectrum under the shot-noise limited condition is

$$\begin{aligned} A_{x,sh}(f) &= \sqrt{\underbrace{2}_{\text{rmsto peak}} \times \underbrace{2}_{\text{double to single sided}} \times S_x(f)} \\ &= \frac{\lambda}{2\pi}\frac{1}{\sqrt{2B\cdot CNR}} = \frac{\lambda}{4\pi}\frac{\sqrt{q}}{\eta_h E_S} \qquad [m/\sqrt{Hz}] \end{aligned} \tag{15}$$

So, the minimum detectable displacement under a given bandwidth Δf is given by

$$\begin{aligned} A_{min} &= A_{x,sh}(f)\cdot\sqrt{\Delta f} \\ &= \frac{\lambda}{4\pi}\frac{\sqrt{q\Delta f}}{\eta_h E_S} \qquad [m] \end{aligned} \tag{16}$$

The SNR of demodulated signal can be explained in Fig. 5(a) under high CNR assumption,

$$SNR = \frac{E[|\theta_{max}|^2]}{\theta_n^2} = \beta^2\cdot CNR \tag{17}$$

but for the case of weak CNR, the nonlinear effect of the demodulator becomes significant, and hence the demodulated noise becomes complicated [26,27]. The performance of the vibrometer is determined by the demodulated SNR, which is relevant to the collected light intensity and definition of the bandwidth. Increasing the transmitted power or designing a large-diameter telescope with better focus ability and limiting the signal bandwidth are effective ways to improve SNR. Note that the influence of the speckle fluctuation and the focused spot size should be carefully traded off, in the meanwhile the limiting bandwidth and the peak frequency deviation βf_m should also be treated carefully.

3. Experiment

An all-fiber 1.55 μm pulsed monostation LDV was implemented with the configuration depicted in Fig. 6. The laser source is a narrow-linewidth (2.4 kHz) semiconductor laser with a 20 mW output power. A 1 × 2 fiber coupler split the laser output to a transmit arm and a LO arm. All the elements are connected using Corning SMF-28 single-mode fiber. In the transmitted arm, a Gooch&Housego AOM, whose RF driver is driven by pulses with 50 ns pulse width and 1 MHz PRF, introduces a 40 MHz frequency upshift. In a continuous wave (CW) mode, the output power at the fiber pigtail is measured to be 5 mW. By calculation, the 5% duty cycle modulation directly results in a pulse energy of 0.25nJ per pulse. The pulse width of 50 ns, corresponds to 7.5 m minimum operation range. If the target is located closer than 7.5 m to the system, the return pulses may superimpose with each other and to make determination of the return pulse position unsuccessful. In order to exclude the distance ambiguity, the 1 MHz PRF corresponds to a maximum operation range 150 m. The 40 MHz frequency shift enables two cycle period in heterodyne signal, which can be easily detected by the envelope detector. After passing through a circulator which is used for monostatic configuration, the pulsed laser beam is focused onto the surface by a zooming telescope. The backscattered speckle field is received by the same optic channel and coupled with the LO in a 2 × 2 50/50 fiber coupler and then feed into the balanced photodetector which can get a good common-mode extinction. After the balanced detector, the analog-to-digital (ADC) converter followed by a RF amplifier which bring the signal level to middle of the peak-to-peak input range of the ADC. The ADC was clocked at 250 MS/s to have the sample rate six times greater than the carrier frequency, which enables a substantially complete waveform of a cycle. In order to validate the proposed pulsed LDV approach, the following typical applications are considered below: (i) range-finding capability; (ii) vibration sensing corresponding to a narrowband tone burst excitation and (iii) vibration sensing due to a wideband speech sample excitation. Fig. 7 presents the system implementation and experimental setup where the surface vibrations were excited with an external acoustic field. As detailed in Fig. 7, the diffused surface located 23 m away from the LDV is vibrated by a loudspeaker several hundreds of mm away.

The basic function of the pulsed mode is range finding, which is relied on the principle of time-of-flight (TOF). Range finding capability is first used in the range gated signal generator. More details about range finding will be presented below. The range resolution of the TOF technique is typically expressed as

$$\delta R = \frac{t_p}{2}\cdot c \tag{18}$$

Because the envelope shown in Fig. 8(b) has a smooth-curved shape, it is possible to estimate the range by calculating the delay between envelope peaks. Sampling at 250 Ms/s, the time resolution reduced from 50 ns to 4 ns (7.5 m to 0.6 m). The histogram of range estimation of a 5 ms duration data, see Fig. 9, shows a ~m ranging capability.

The pulses in the buffered range-Doppler matrix (see Fig. 8(a)) are “incoherent” for the phases in the slow-time direction are moving backwards. Triggered jitter error of the pulse generator and ADC can delay every pulse a little fixed phase step, which accounts for the phase ripple in buffered range-Doppler matrix. In a traditional pulsed Doppler radar, the ”coherent” pulses share the same initial phase for a stationary target, while these phase-stepping pulses have a varying initial phase in slow time axis (see Fig. 8(c)). Demodulation of these step-varying

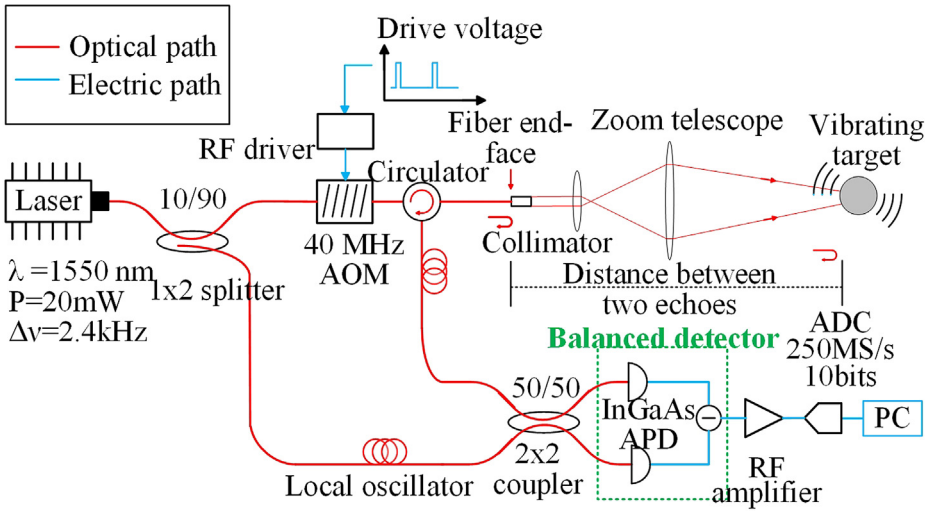

Fig. 6. Diagram of Experimental architecture allowing pulse operation. The laser source is a 20 mW single-mode fiber laser (ECWL-SF-P20) with a narrow line width of 2.4 kHz from HFB PHOTONICS. The acousto-optic modulator is a fiber-coupled AOM working at 40 MHz from Gooch&Housego. The drive voltage is supplied by a AFG3000C Arbitrary/Function Generator from Tektronix. The detector is an auto-balanced detector with avalanche photodiodes (PDB570C) from Thorlabs. The ADC is sampled at 250 MS/s by a NI-PCIe 5162 with a 10 bits quantification.

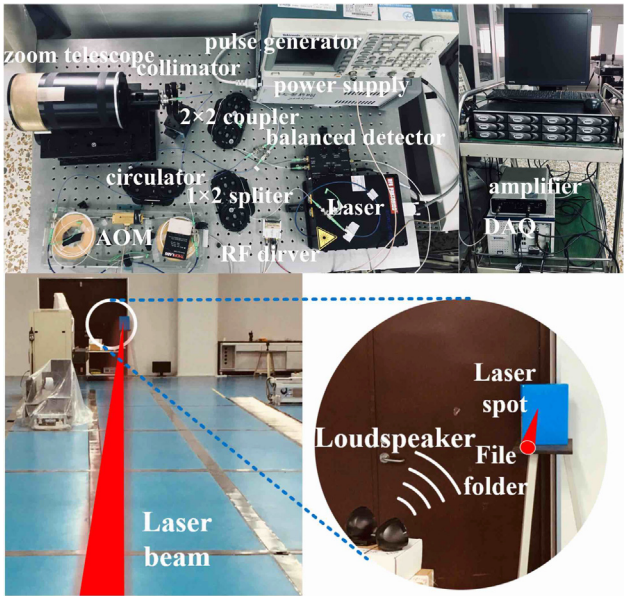

Fig. 7. System implementation and experimental setup.

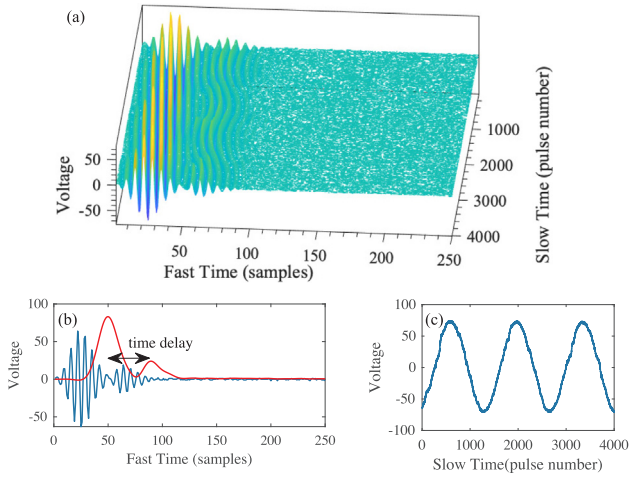

Fig. 8. (a) 3D plot of the buffer matrix (b) pulse waveform and envelope in fast time axis (c) Phase variation in slow time axis at the 25th fast time sample.

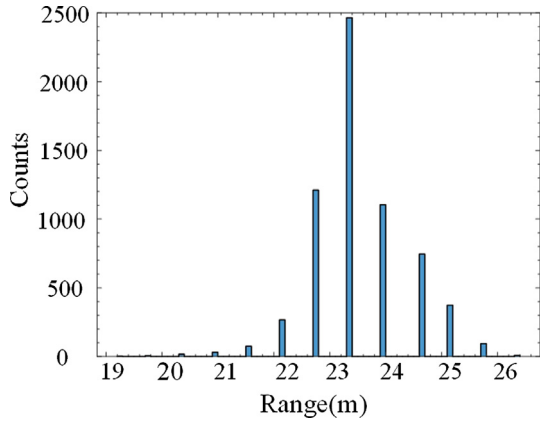

Fig. 9. Histogram of range estimation during 5 ms measurement time using the subtraction of the envelope peak position within one pulse interval.

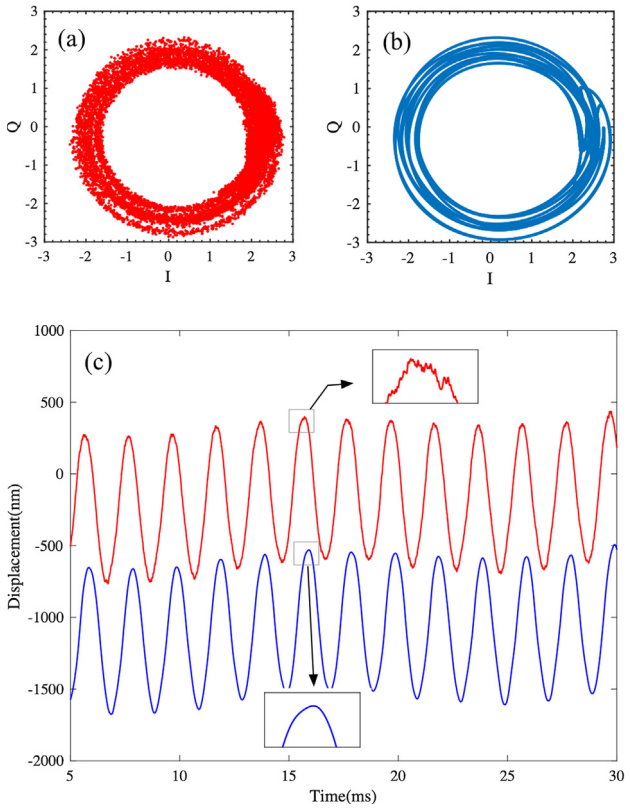

Fig. 10. Experimental results for a single frequency at 500 Hz: (a) and (b) Lissajous scatters without and with final antialiasing low-pass filter (cutoff frequency = 3 kHz), respectively. (c) Demodulated displacements without (red) and with (blue) the filter.

phases can bring a spurious vibration which is a ~700 Hz tone vibration corresponding to the 1400 μs period in Fig. 8(c).

A vibrometer capability is the main function of the LDV system. To demonstrate its vibrometer capability experimentally, we use a sinusoidal vibration (f_m = 500 Hz, $A_{vib,max}$ ≅ 500 nm) and acoustic signal to verify and test its normal function. As shown as Fig. 10, the Lassajous trajectory of the I & Q scatters with a narrower filter has a better circle profile than the one without the filter, which means a narrow bandwidth can improve the SNR. Correspondingly, the demodulated displacement curves (blue) with the filter has a smoother curve than that without filter (red). A velocity can be calculated by phase difference. Fig. 11 shows the amplitude spectrum of surface displacement and

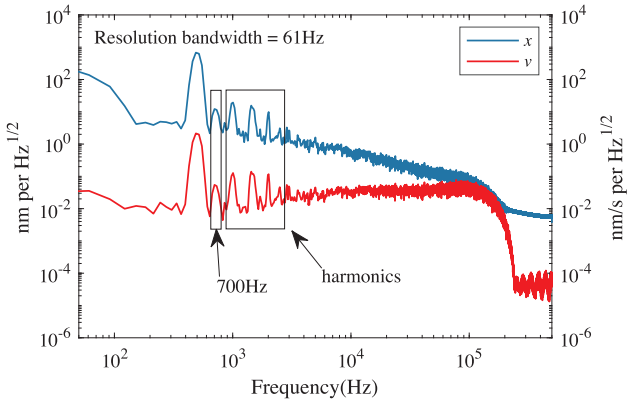

Fig. 11. Amplitude spectrum of surface displacement (blue) and velocity (red) without antialiasing filter. (For interpretation of the references to color in this figure legend, the reader is referred to the web version of this article.)

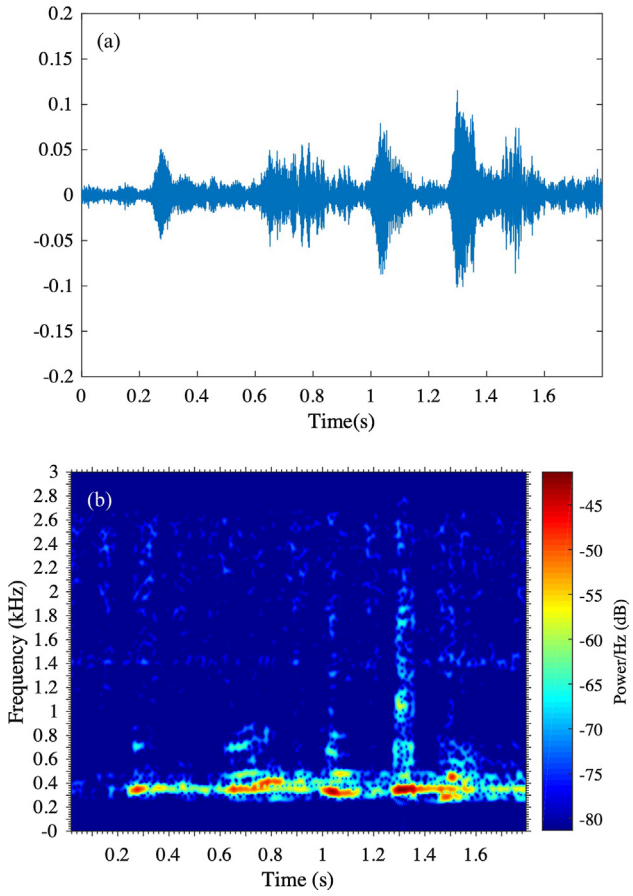

Fig. 12. Acoustic reconstruction of forced vibration of the diffuse surface (The speech content is "Chinese Academy of Sciences" in Chinese). (a) Waveform (b) spectrogram.

velocity without the antialiasing filter. The spectrum is obtained by dividing the signal into segment of 16384 samples (bandwidth = 61 Hz) with 50% overlapping and calculating the discrete Fourier transform with a hamming window applied. The single tone of 500 Hz and its harmonics are clearly illustrated with a 700 Hz distortion component (due to the "incoherent" pulse caused by the trigger jitter). The picture indicates the displacement amplitude noise spectrum is proportional to f^{-1}, while the velocity amplitude noise spectrum is flat below f_{exc} and $1/f$ above f_{exc}. The result is agreed well with Dräbenstedt's results [25]. The difference in the shot noise region is oscillating rather climbing in contrast with [23]. This oscillating is caused by the laser feedback in absence of an isolator. Because the acoustic region is far away from the shot noise region, the vibration of interest is almost unaffected. The acoustic signal is reconstructed through a bandpass filter (300 Hz ~ 3 kHz) in Fig. 12(a). The spectrogram of the acoustic signal, graphed in Fig. 12(b), has a concentrated energy distribution between 300 Hz and 500 Hz, which is related to the vibration response characteristics of diffused targets.

4. Conclusion and future work

We have demonstrated a monostatic pulsed laser Doppler vibrometer using a digital signal processing method, which can eliminate cochannel interference and improve the SNR of demodulated signal. By modulating the AOM, the sounding pulse has an ultra-low energy which is about 0.25 nJ. The prototype reconstructed single frequency vibration and acoustic vibration successfully at a 23 m stand-off. A more pulse energy implementation by adopting an power amplifier based on Master Oscillator Power-Amplifier (MOPA) configuration is able to detect a longer distance vibration. Compared with a conventional LDV, the pulsed all-fiber one is more compact in structure and lower-cost in levering the off-of-shelf optical communication device. In addition, it needs no more complex optical design and aligning. Further work on signal processing based on embedded processors such as FPGA (Field Programmable Gate Array), ARM (Advanced RISC Machines), DSP (Digital Signal Processing) can be accelerated with the help of the state-of-art hardware and software capability. The success of the demonstration can be meaningful to achieve a high-performance low-cost design within stringent SWaP budgets. And, it is easy to integrate multi-functional ability to range finding, vibrometry, video tracking, intelligent recognition, and so on.

Declaration of Competing Interest

The authors declare that they have no known competing financial interests or personal relationships that could have appeared to influence the work reported in this paper.

Acknowledgement

This work was sponsored by National Natural Science Foundation of China (No. 61805234 and No. 51905482), Key Research Program of Frontier Science, CAS (No. QYZDB-SSWSLH014) and the Foundation of State Key Laboratory of Laser Interaction with Matter (No. SKLLIM1704).

References

[1] C. Cristalli, B. Torcianti, J. Vass, A new method for filtering speckle noise in vibration signals measured by laser doppler vibrometry for on-line quality control, Seventh International Conference on Vibration Measurements by Laser Techniques: Advances and Applications, vol. 6345, International Society for Optics and Photonics, 2006, p. 63450Y.
[2] J. Vass, R. Šmíd, R. Randall, P. Sovka, C. Cristalli, B. Torcianti, Avoidance of speckle noise in laser vibrometry by the use of kurtosis ratio: application to mechanical fault diagnostics, Mech. Syst. Signal Process. 22 (3) (2008) 647–671.
[3] R.R. Ebert, P. Lutzmann, Vibration imagery of remote objects, Free-Space Laser Communication and Laser Imaging II, vol. 4821, International Society for Optics and Photonics, 2002, pp. 1–11.
[4] Y. Mizuno, N. Hayashi, H. Fukuda, K.Y. Song, K. Nakamura, Ultrahigh-speed distributed brillouin reflectometry, Light: Sci. Appl. 5 (12) (2016) e16184.
[5] V. Jolivet, P. Gueguen, et al., On the full scale dynamic behaviour of rc-buildings using coherent laser radar vibrometer, in: 14th World Conf. on Earthquake Engineering, 2008.
[6] P. Gueguen, V. Jolivet, C. Michel, A.-S. Schveitzer, Comparison of velocimeter and coherent lidar measurements for building frequency assessment, Bull. Earthq. Eng. 8 (2) (2010) 327–338.
[7] J. Shang, Y. He, D. Liu, W. Chen, Laser doppler vibrometer for long-distance acoustical signals acquirement, in: Conference on Lasers and Electro-Optics/Pacific Rim, Optical Society of America, 2009, p. TuE1_6.
[8] W. Li, M. Liu, Z. Zhu, T.S. Huang, Ldv remote voice acquisition and enhancement, 18th International Conference on Pattern Recognition (ICPR'06), vol. 4, IEEE, 2006, pp. 262–265.
[9] N. Roozen, L. Labelle, M. Rychtáriková, C. Glorieux, Determining radiated sound power of building structures by means of laser doppler vibrometry, J. Sound Vib. 346 (2015) 81–99.
[10] N. Roozen, L. Labelle, Q. Leclere, K. Ege, S. Alvarado, Non-contact experimental assessment of apparent dynamic stiffness of constrained-layer damping sandwich plates in a broad frequency range using a nd: Yag pump laser and a laser doppler vibrometer, J. Sound Vib. 395 (2017) 90–101.
[11] C.J. Karlsson, F.Å. Olsson, D. Letalick, M. Harris, All-fiber multifunction continuous-wave coherent laser radar at 1.55 μm for range, speed, vibration, and wind measurements, Appl. Opt. 39 (21) (2000) 3716–3726.
[12] C.A. Hill, M. Harris, K.D. Ridley, E. Jakeman, P. Lutzmann, Lidar frequency modulation vibrometry in the presence of speckle, Appl. Opt. 42 (6) (2003) 1091–1100.
[13] J.R. Rzasa, K. Cho, C.C. Davis, Long-range vibration detection system using heterodyne interferometry, Appl. Opt. 54 (20) (2015) 6230–6236.
[14] A. Dräbenstedt, J. Sauer, C. Rembe, Remote-sensing vibrometry at 1550 nm wavelength, in: AIP Conference Proceedings, vol. 1457, AIP, 2012, pp. 113–121.
[15] A. Denisov, M.A. Soto, L. Thévenaz, Going beyond 1000000 resolved points in a brillouin distributed fiber sensor: theoretical analysis and experimental demonstration, Light: Sci. Appl. 5 (5) (2016) e16074.
[16] A. Waz, P. Kaczmarek, K. Abramski, Laser–fibre vibrometry at 1550 nm, Meas. Sci. Technol. 20 (10) (2009) 105301.
[17] M. Harris, G. Constant, C. Ward, Continuous-wave bistatic laser doppler wind sensor, Appl. Opt. 40 (9) (2001) 1501–1506.

[18] J. Totems, V. Jolivet, J.-P. Ovarlez, N. Martin, Advanced signal processing methods for pulsed laser vibrometry, Appl. Opt. 49 (20) (2010) 3967–3979.
[19] S. Kameyama, T. Ando, K. Asaka, Y. Hirano, S. Wadaka, Compact all-fiber pulsed coherent doppler lidar system for wind sensing, Appl. Opt. 46 (11) (2007) 1953–1962.
[20] M.P. Dierking, B.D. Duncan, Periodic, pseudonoise waveforms for multifunction coherent ladar, Appl. Opt. 49 (10) (2010) 1908–1922.
[21] R. Lyons, Digital envelope detection: The good, the bad, and the ugly [tips and tricks], IEEE Signal Process. Mag. 34 (4) (2017) 183–187.
[22] J.E. Posada-Roman, D.A. Jackson, J.A. Garcia-Souto, Variable configuration fiber optic laser doppler vibrometer system, Photonic Sens. 6 (2) (2016) 97–106.
[23] L.A. Jiang, M.A. Albota, R.W. Haupt, J.G. Chen, R.M. Marino, Laser vibrometry from a moving ground vehicle, Appl. Opt. 50 (15) (2011) 2263–2273.
[24] W.J. Warren, E.A. Moro, M.E. Briggs, E.B. Flynn, Simulating translation-induced laser speckle dynamics in photon doppler velocimetry, Appl. Opt. 53 (21) (2014) 4661–4668.
[25] A. Dräbenstedt, Quantification of displacement and velocity noise in vibrometer measurements on transversely moving or rotating surfaces, in: Optical Measurement Systems for Industrial Inspection V, vol. 6616, International Society for Optics and Photonics, 2007, p. 661632.
[26] K. Ridley, E. Jakeman, Signal-to-noise analysis of fm demodulation in the presence of multiplicative and additive noise, Signal Process. 80 (9) (2000) 1895–1907.
[27] K. Ridley, E. Jakeman, Fm demodulation in the presence of multiplicative and additive noise, Inverse Problems 15 (4) (1999) 989.